Ceramics International 48 (2022) 4904–4910

Contents lists available at ScienceDirect

Ceramics International

journal homepage: www.elsevier.com/locate/ceramint

Anisotropic strength and fracture resistance of epoxy-ceramic composite materials produced by ultrasound freeze-casting

Carina B. Tanaka [a], Max Mroz [b], Steven E. Naleway [b], Jamie J. Kruzic [a,*]

[a] School of Mechanical and Manufacturing Engineering, University of New South Wales (UNSW Sydney), Sydney NSW 2052, Australia
[b] Department of Mechanical Engineering, University of Utah, 1495 East 100 South, 1550 MEK, Salt Lake City, UT, 84112, USA

ARTICLE INFO

Keywords:
Freeze casting
Ceramic scaffolds
Composites
Strength
Fracture toughness
Ultrasound

ABSTRACT

The anisotropic mechanical properties of ultrasound freeze cast epoxy-ceramic composite materials were studied by measuring flexural strength and fracture resistance curves (R-curves) using both unnotched and notched three-point beam bending experiments, respectively, cut in three different orientations relative to the directional freezing axis. Three ultrasound frequencies of 0.699, 1.39 and 2.097 MHz were used in order to introduce different length scales into the microstructure, with 0 MHz used as the control samples. For all cases, the composites showed higher strength and fracture resistance when the crack plane cut across the direction of ice growth (denoted as the YX orientation). The anisotropic properties were more evident for the material produced without ultrasound (0 MHz) where the flexural strength was approximately 160% higher for the YX orientation compared to two orthogonal orientations. Most of the fracture resistance increase was found to occur within a crack extension, Δa, of ~0.5 mm. Comparing the fracture resistance at $\Delta a = 0.5$ mm for the highly anisotropic 0 MHz samples showed that the YX orientation was approximately 86% tougher than the two orthogonal orientations. When the ultrasound operation frequencies of 0.699, 1.39 and 2.097 MHz were applied, the amount of anisotropy in the strength and fracture resistance gradually decreased as the operating frequency increased. The high strength and fracture resistance for the YX orientation was attributed to the alignment of the ceramic particles along the freeze front direction creating a barrier for crack propagation. Ultrasound modifies the material microstructure, introducing relatively dense ceramic layers perpendicular to the freezing front direction that act as an additional, orthogonal barrier to crack propagation. The addition of the denser layers acts to improve the mechanical properties in the weaker orientations and reduce the overall anisotropy.

1. Introduction

The freeze-casting fabrication process has been extensively studied over the past 20 years for its ability to fabricate tailored, porous ceramic materials and composites with hierarchical microstructures. These novel materials have a variety of potential applications such as biomedical implants [1–3], energy materials [4–6], and impact resistant porous ceramics [7–9]. The porous structure of the freeze-cast ceramic is critical for each of these applications; however, due to their brittle nature and high porosity, their low fracture resistance is often a limiting factor for practical applications.

The freeze-casting process consists of four steps [10–15]: (1) a colloidal slurry is mixed containing solid loading particles (e.g., ceramic particles) and a freezing agent (e.g., liquid water), along with polymeric binders and dispersants, (2) the colloidal slurry is directionally frozen, allowing for the dendritic growth of ice crystals to segregate and template the solid particles, (3) the frozen slurry is sublimated to remove the frozen freezing agent without altering the templated structure of the solid particles, thus creating a green body, and (4) the green body is densified (e.g., sintered) to form a final, solid freeze-cast material where the resultant porosity is the negative of the ice dendrites. In addition, many reports on freeze casting include a fifth, post-processing step where the freeze-cast samples are infiltrated with a second polymeric [16–18] or metallic phase [19–22] to produce a composite material.

Given that the critical fabrication step (step (2) above) in freeze casting occurs while the solid loading particles are unconstrained and suspended in a liquid medium, a number of techniques that employ external energized fields have been reported to provide additional control over the structure and properties of the resultant freeze-cast materials. These include the application of electric [23,24], magnetic

* Corresponding author. School of Mechanical and Manufacturing Engineering, UNSW Sydney, Sydney NSW 2052, Australia.
E-mail address: j.kruzic@unsw.edu.au (J.J. Kruzic).

https://doi.org/10.1016/j.ceramint.2021.11.027
Received 15 August 2021; Received in revised form 18 October 2021; Accepted 3 November 2021
Available online 5 November 2021

[7,25–27], and ultrasonic [28,29] fields. These techniques allow for user-tailored microstructures to be produced within the final freeze-cast materials. Of particular interest in terms of the fracture toughness is ultrasound freeze casting, which has recently been shown to create a layered structure that shows a density variation orthogonal to the freezing direction and was shown to raise the flexural strength by ~50% for fracture across the layers [28].

Many biological materials such as dentin, bone, abalone shells, and eggshells show variations in their fracture resistance based on their highly directional microstructural features [30–33]. For example, eggshell is composed of calcite crystals organized in a columnar structure oriented from the interior to exterior of the shell. These calcite crystals result in toughness that is significantly higher when the crack propagates across the calcite crystals as compared to when crack propagation occurs parallel to the calcite crystals, which causes the calcite crystals to separate [31].

Given that the microstructural anisotropy of freeze-cast materials is often developed to mimic biological materials [11,25], it is logical to find similar anisotropy in their mechanical properties. The natural microstructural alignment of freeze-cast materials along the freezing direction often causes high mechanical strength in a single loading orientation, with much lower strengths in the two orthogonal loading directions [34]. While this strength anisotropy effect is well known for freeze-cast materials, the strength of brittle ceramics is actually governed by the fracture resistance which is best described by fracture resistance curves (*R*-curves) [35]. In this regard, the *R*-curve behavior of freeze cast materials has generally only been reported for loading direction perpendicular to the microstructural alignment along the freezing direction [21,36–39], which would naturally be the toughest. Furthermore, strong mechanical anisotropy creates many challenges for engineering design, i.e., one must ensure that the applied loading always occurs as designed or else unexpected failure might occur in a weak orientation. To mitigate strong anisotropy, ultrasound freeze casting has been demonstrated to impart microstructural organization into freeze-case materials oriented orthogonal to the freezing direction [28,29], thus providing a potential pathway to a more isotropic material response.

Accordingly, the object of this work is to provide a first study of the strength and fracture resistance (i.e., *R*-curve) anisotropy for ultrasound freeze-cast materials produced with various ultrasound frequencies. It is hypothesized that ultrasound freeze casting will improve the mechanical properties of the weaker orientations, resulting in a more isotropic mechanical response compared to a similar material produced by conventional freeze casting with no ultrasonic field.

2. Materials and methods

2.1. Freeze-casting sample preparation

The ultrasound freeze-casting process used in the present study was previously developed by Mroz et al. [28]. Freeze-cast slurries were prepared by combining 10 vol% TiO_2 (particle size <500 nm, ACROS Organics, Pittsburgh, PA, USA) with 1 wt.% Darvan 811 as a dispersant (R.T. Vanderbilt Company Inc., Norwalk, CT, USA), 0.22 vol% 1-Octanol as an antifoaming agent (Sigma-Aldrich, St. Louis, MO, USA), and 1 wt.% polyethylene glycol (PEG, MW = 10,000 g/mol, Alfa Aesar, Ward Hill, MA, USA) and 1 wt.% polyvinyl alcohol (PVA, MW = 88,000–97,000 g/mol, Alfa Aesar, Ward Hill, MA, USA) as binders. Titanium oxide (TiO_2) particles were used in the present investigation due to their good biocompatibility, non-toxicity, and corrosion resistance properties that make them attractive for potential biomaterials applications. These components were mixed with distilled water and ball milled for 16 h. Directly after ball milling, the freeze-cast slurries were poured into a custom ultrasound freeze casting fabrication setup, as described in our previous work [28]. Freeze-cast slurries were frozen at a rate of 10 °C/min while applying ultrasound waves. Commercial piezoelectric plates with center frequencies of 0.710 MHz, 1.5 MHz, and 2.0 MHz were operated at ultrasound operating frequencies of 0 MHz (no applied ultrasound), 0.699 MHz, 1.390 MHz, and 2.097 MHz, respectively. Note that these operating frequencies were chosen to match previous results and allow for comparisons [28]. The ultrasound transducer was placed on top of the slurry reservoir and the ultrasound was applied throughout the entire freezing process. The direction of the ultrasound wavefield propagation was opposite to the ice crystal growth direction (Fig. 1). After completely freezing, the frozen specimens were sublimated in a freeze drier (Labconco FreeZone 1, Labconco Corporation, Kansas City, MO, USA) for 48 h to fully remove the ice, then they were sintered in an open-air furnace (Keith KSK-121,700, Keith Company, Pico Rivera, CA, USA) at 925 °C for 3 h with heating and cooling rates of 2 °C/min. After sintering, the scaffolds were vacuum infiltrated at a pressure of 5 Pa with a two-part epoxy (EpoxiCure 2 resin, Buehler, Lake Bluff, IL, USA) and allowed to cure for 24 h at room temperature (20 °C). The resultant freeze-cast samples were TiO_2-epoxy composites that were 22 × 16 × 22 mm^3. In total, 24 freeze-cast samples were fabricated, six each at 0 MHz, 0.699 MHz, 1.390 MHz, and 2.097 MHz.

2.2. Flexural strength

Unnotched beams nominally 22 × 3.5 × 2.5 mm^3 were cut for flexural strength testing using a low-speed diamond saw (Minitom, Struers, Denmark) with their length dimension either parallel (in each of the two orthogonal directions) or perpendicular to the freezing direction. See Fig. 1 for details of the three sample orientations compared in this study. For the XY oriented samples, fracture of the specimens progressed in a direction parallel to the freeze front while for the XZ and YX oriented samples fracture of the specimens cut across the freeze front as visualized by the notches shown in Fig. 1. Since flexural strength data for the XY orientation was previously reported in Ref. [28], only the YX and XZ orientations were tested for strength in the present study using similar test conditions. The surfaces of the specimens were wet ground with P1200, P2400 and P4000 grit silicon carbide paper. The samples (n = 10) were tested in a three-point bending setup using a Deben MICROTEST 2 kN bending stage (Deben UK Ltd, London, UK) with a loading span of L = 20 mm, roller diameter of 2 mm, a 150 N capacity calibrated load cell, and a crosshead speed of 0.2 mm/min. Flexural strength, *FS*, was calculated according to Ref. [40]:

$$FS = \frac{3PL}{2BW^2} \quad (1)$$

where P was the applied load at fracture. The sample thickness, B, and the sample width, W, were nominally 3.5 mm and 2.5 mm, respectively.

2.3. R-curve measurements

To determine *R*-curves, fracture resistance, K_R, was measured as a function of crack extension, Δa, using single edge V-notch beam (SEVNB) specimens (width, $W \approx 4$ mm; thickness, $B \approx 2$ mm) that were cut from the ultrasound freeze cast epoxy-ceramic composite blocks. The beams were cut in the same orientations as described in section 2.2 and as shown in Fig. 1. The notches were made such that for the XY orientation the crack propagated parallel to the freeze front, and for the XZ and YX orientations the cracks propagated across the freeze front (Fig. 1). Each specimen was razor micronotched using a custom-built rig to slide a razor blade back-and-forth across the samples while being irrigated with a 1 μm diamond suspension (DP-Paste M, Struers, Denmark) and lanolin lubricant to produce a sharp V-notch with an average length of 465 ± 97 μm. The surfaces of the specimens were wet ground with P1200, P2400 and P4000 grit silicon carbide paper to allow for observations of the cracking process.

The *R*-curves were measured under a digital optical microscope (AxioZoom.V16, Zeiss, Germany) using a Deben MICROTEST 2 kN

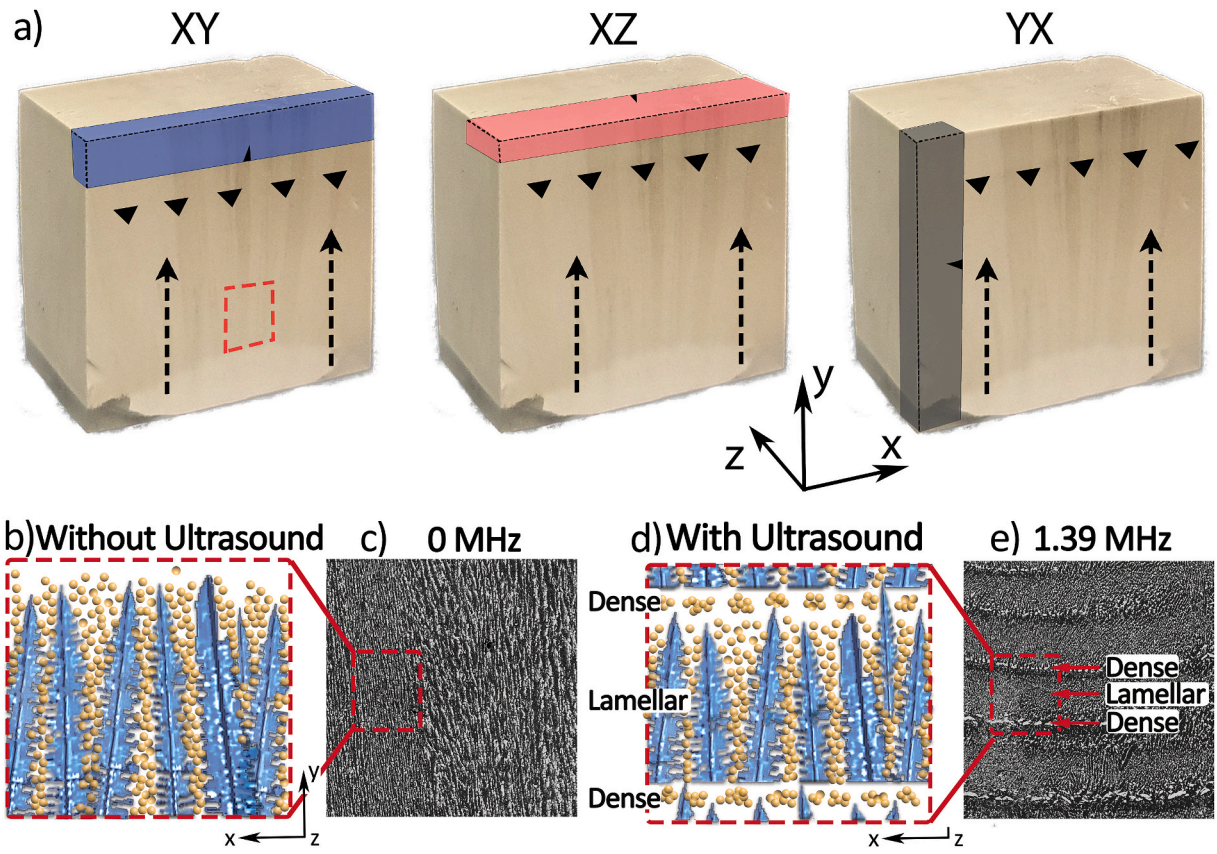

Fig. 1. a) Different sample orientations XY, XZ, and YX are shown along with the coordinate system, the direction of the freeze front (upward dashed arrows, y-direction) and the propagation direction of the ultrasound wavefield (downward triangles). The sample naming convention is: *First letter*: crack plane orientation, which is the coordinate axis direction perpendicular to the crack plane; and *Second letter*: the crack propagation direction. Comparison schematics and SEM images of the epoxy-ceramic composite microstructures b), c) without (0 MHz) and d), e) with an ultrasound operating frequency. e) shows the alternating dense and lamellar layers that formed due to an ultrasound operating frequency of 1.39 MHz. The spacing between adjacent dense and lamellar layers decreases with increasing ultrasound operating frequency as described in detail in Ref. [28].

bending stage (Deben UK Ltd, London, UK). For most tests a 20 mm loading span was used. However, due to a shorter initial block length for the 0.699 MHz samples in the Y-direction, a shorter loading span of 16 mm was used for the YX oriented samples. Three samples (n = 3) were tested for each combination of ultrasound frequency and samples orientation. The optical microscope was used to ensure that the specimen was well aligned in the bending fixture and to monitor the crack propagation during testing. Samples were gradually loaded using displacement control until the onset of sub-critical cracking was observed in the microscope. The samples were unloaded by about 15–20% of the maximum load and then were reloaded until subsequent crack extension and this process was repeated to measure fracture resistance as a function of crack extension. Real-time images were recorded at a magnification of 100x. Multiple images were stitched together using Adobe Photoshop 2020 and the crack lengths, a, were calculated from the stitched images. The fracture resistance, K_R, at each new crack length was calculated according to the stress intensity factor equation for the SEVNB sample geometry:

$$K_R = \frac{PL}{BW^{3/2}} x \frac{3\left(\frac{a}{W}\right)^{1/2}\left[1.99 - \frac{a}{W}\left(1-\frac{a}{W}\right)\left\{2.15 - 3.93\left(\frac{a}{W}\right) + 2.7\left(\frac{a}{W}\right)^2\right\}\right]}{2\left(1+2\frac{a}{W}\right)\left(1-\frac{a}{W}\right)^{3/2}} \quad (2)$$

where P is the load required to achieve a given crack length, a, while L is the length of the support span, and B and W are the specimen thickness and width, respectively.

The R-curve data was fit according to Ref. [41]:

$$K_R = K_{I0} + C_1\left(1 - \left(1 + C_2\sqrt{\delta a}\right)\exp\left[-C_2\sqrt{\delta a}\right]\right) + C_3\left(1 - \left(1 + C_4\sqrt{\delta a}\right)exp\left[-C_4\sqrt{\delta a}\right]\right) \quad (3)$$

In Eq. (3), K_{I0} is the initiation toughness of the R-curve which should be representative of the intrinsic toughness of the material in the absence of extrinsic toughening by crack deflection and bridging; thus, it should be approximately identical for all cases. K_{I0} was deduced to be ~0.35 MPa$\sqrt{m}$ based on extrapolating the conventionally freeze cast (0 MHz) sample data back to zero crack extension. Finally, the "best fit" set of coefficients (C) were calculated using the method of least squares to fit the data up to ~2 mm of crack extension.

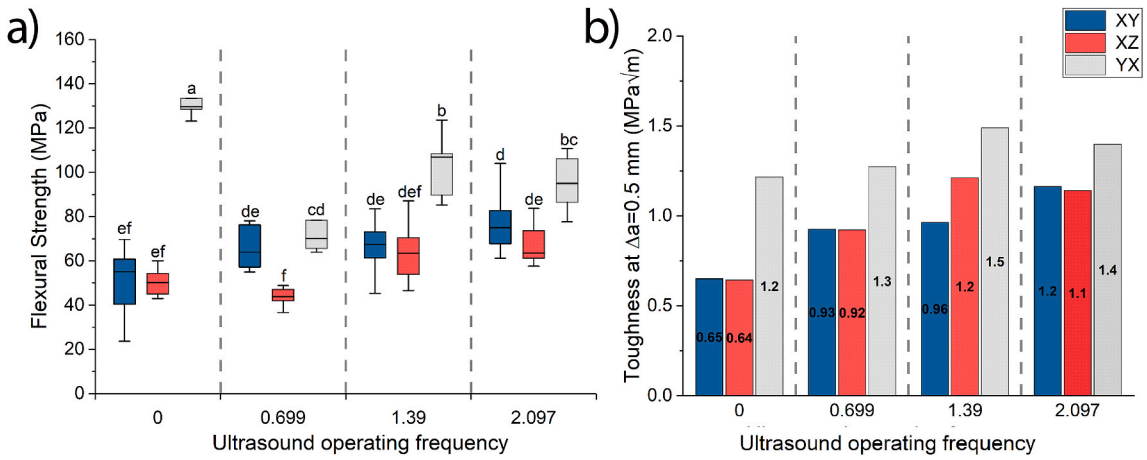

Fig. 2. a) Mean flexural strength and b) toughness values at $\Delta a = 0.5$ mm taken from the *R*-curve fit lines shown in Fig. 3. The flexural strength data plotted for the XY orientation are reproduced from Ref. [28] while the flexural strength data for the XZ and YX orientations were obtained in the present study using similar testing conditions. In a) data in the box is presented as 25–75% with a median line. The whiskers represent the 5 to 95 percentile range. Identical letters in a) indicate no statistically significant flexural strength difference ($p > 0.05$) between the groups. For details of the sample orientations refer to Fig. 1.

2.4. Statistical analyses

A two-way analysis of variance (ANOVA) was performed on the flexural strength data to determine if sample orientation (XZ, YZ, ZX) and ultrasound frequency (0, 0.699, 1.39 and 2.097 MHz) had a statistically significant effect on the values using the software package Minitab (Minitab, LLC., State College, PA, USA). Pairwise comparisons were made using Tukey's post-hoc test and in all cases $p < 0.05$ was considered statistically significant.

3. Results

The mean flexural strength results are presented in Fig. 2a. The two-way ANOVA showed a statistically significant effect ($p < 0.001$) of both ultrasound and sample orientation on the mean flexural strength. Pairwise statistical tests revealed that the YX oriented samples generally had higher strength compared with the XY and XZ orientations and also that samples without any applied ultrasound (0 MHz) tested in the YX orientation were significantly stronger than those with applied ultrasound. However, for samples tested in the XY and XZ directions the effect of ultrasound on flexural strength was opposite to the YX orientation

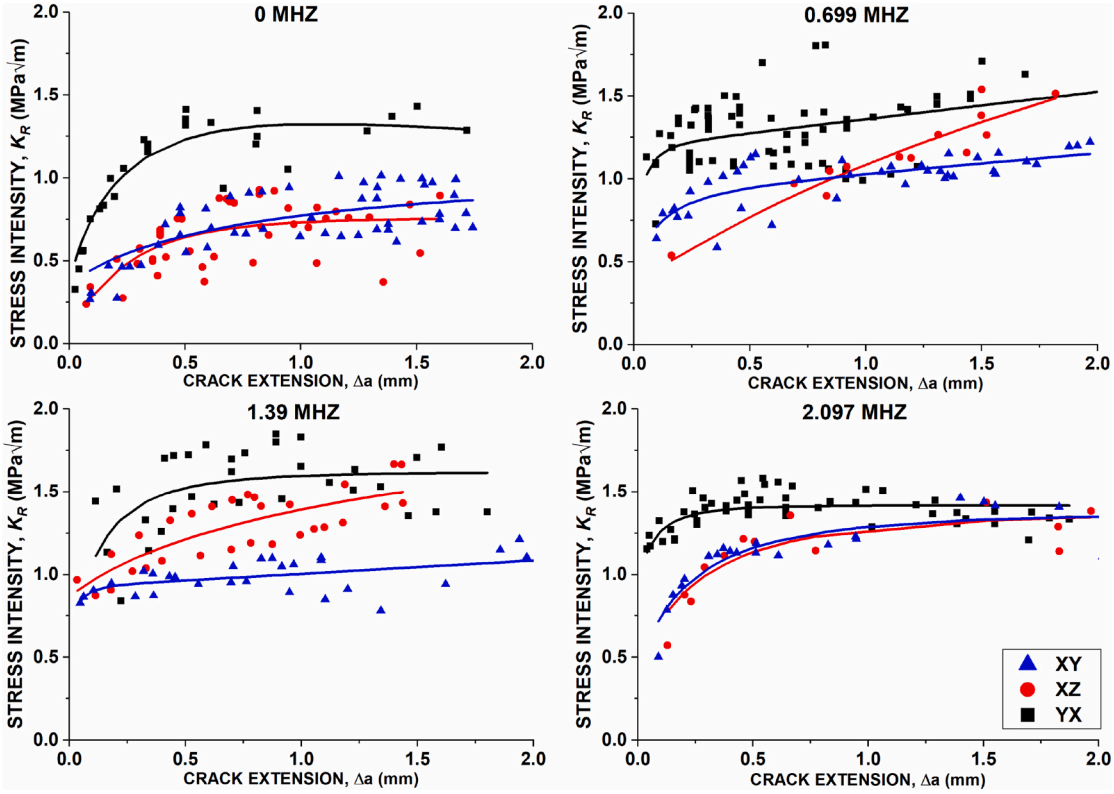

Fig. 3. Resistance-curves, K_R (Δa), measured from three samples for each combination of ultrasound frequency (0, 0.699, 1.39 and 2.097 MHz) and sample orientation (XY, XZ and YX). The fit lines were created by fitting the data points for all three samples together to Eq. (3). For details of the sample orientations refer to Fig. 1.

and a statistically significant ($p < 0.001$) strengthening effect was observed for the 2.097 MHz XY oriented samples compared to the same orientation without applied ultrasound.

The *R*-curves giving the stress intensity required to extend the crack, K_R, as a function of crack extension, Δa are shown in Fig. 3. Overall, the *R*-curves for all sample types rose most significantly at short crack lengths over ~0.5 mm, after which they began to plateau or rise more slowly. Although Fig. 3 shows several different shapes to the *R*-curves, a consistent feature was that most of the toughening occured during the first 0.5 mm of crack extension. Thus, to make fair comparisons across different shaped *R*-curves, we chose to compare the toughness values obtained from the *R*-curve fit lines at 0.5 mm crack extension in Fig. 2b. In all cases, the YX orientation showed higher toughness values compared with the XY and XZ orientations. The fracture resistance at 0.5 mm crack length for the 0 MHz was 86% higher in the YX compared to the XZ and XY orientations. This toughness difference between orientations reduced with higher ultrasound operating frequencies. The toughness in the YX orientation was 41% and 22% higher than the XZ and XY for 0699 MHz and 2.097 MHz, respectively.

Fig. 4 shows the crack propagation process during the *R*-curve measurement of the epoxy ceramic composite structure. For the XY orientation (Fig. 4a) the fracture process occurred in the same direction to the freeze front (dashed arrow in Fig. 1). The crack propagates parallel and between the ceramic columns formed in the Y-direction. In contrast, crack kinking along the ceramic column boundaries can be observed during the fracture process in the XZ direction (Fig. 4b). The highest toughness was observed for the YX direction (Fig. 4c) in which the crack propagated across the ceramic columns created by the ice growth during the fracture process. A more detailed microstructure analysis of the porosity, periodic feature spacing, and feature length of the layered lamellar and dense microstructure has been previously reported in Ref. [28]. To aid the further discussion, we note here that the relatively dense layers contain approximately 20% less porosity compared to the lamellar layers, i.e., ~45% versus ~65% porosity [28].

4. Discussion

One way to quantify the mechanical anisotropy of a material is by the ratio of the mechanical properties for the various orientations. For the present work, the freeze-cast composites exhibit similar strength and fracture toughness values for the two orientations, XY & XZ, where the fracture plane is parallel to the freeze front. Thus, one measure of anisotropy would be the ratio of the YX orientation property to the average of the other two "weak" orientations:

$$\text{Anisotropy Ratio} = \text{AR} = \frac{2\text{YX}}{(\text{XY} + \text{XZ})} \tag{4}$$

In the absence of ultrasound (0 MHz), AR = 2.6 for strength and 1.9 for toughness, indicating the high anisotropy in properties for traditional freeze-case materials. For strength, a trend of increasing strength with ultrasound frequency is seen for the XY & XZ orientations, while for the YX orientation there is a reduction in strength when ultrasound is added (Fig. 2). The net result of these trends is a more isotropic strength response for the ultrasound freeze cast samples with AR decreasing to 1.4, 1.6, and 1.3 for the 0.699, 1.39 and 2.097 MHz samples, respectively.

Similarly, the toughness increased dramatically with increasing ultrasound frequency for the XY and XZ orientations and nearly doubled for the 2.097 MHz samples. In contrast, for the YX orientation the toughness values were less affected by the different ultrasound frequencies (Fig. 2b). Similar to strength, the anisotropy in the toughness response was reduced with ultrasound with AR decreasing from 1.9 for

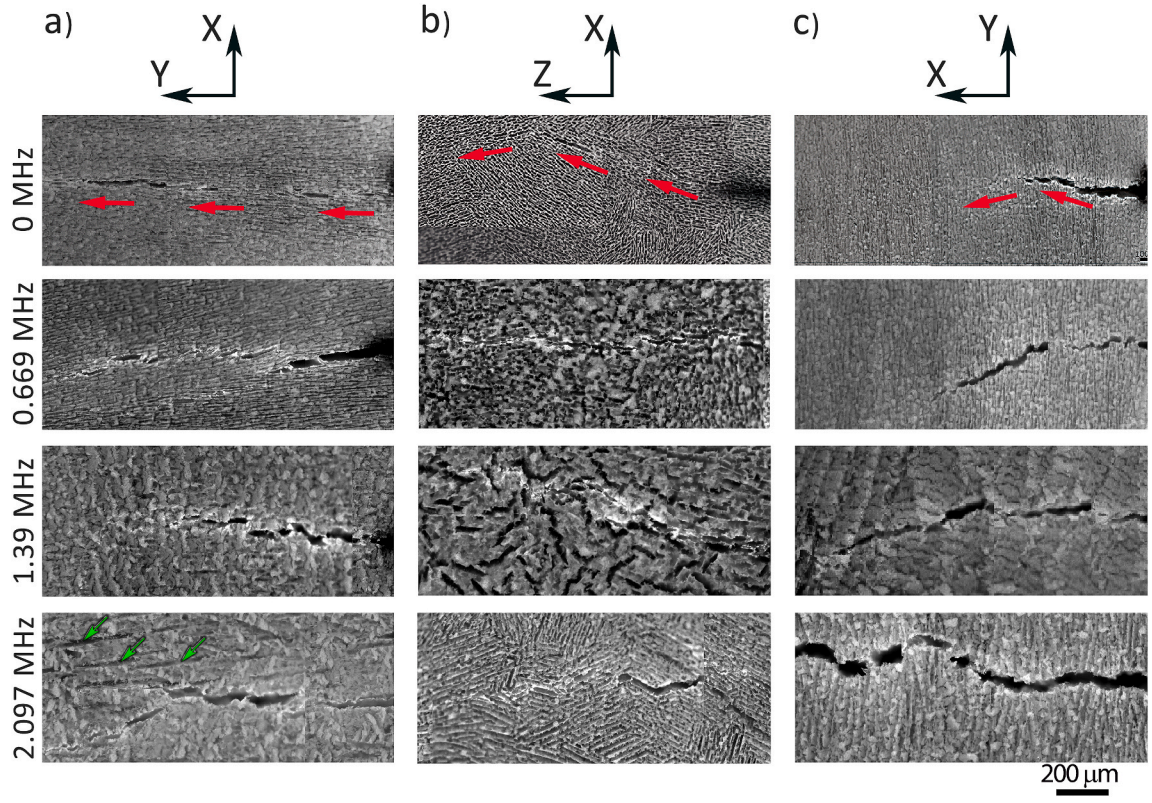

Fig. 4. Optical micrographs taken *in-situ* during the fracture process for the 0, 0.699, 1.39 and 2.097 MHz specimens tested in the a) XY, b) XZ, and c) YX orientations. For details of the sample orientations refer to Fig. 1. Green arrows point out ice templated features that has been infiltrated with epoxy resin. Red arrows show the crack propagation path which was right to left in the micrographs. (For interpretation of the references to colour in this figure legend, the reader is referred to the Web version of this article.)

0 MHz to 1.4 for both 0.699 and 1.39 MHz and 1.2 for 2.097 MHz. Thus, the hypothesis that ultrasound freeze casting can improve the mechanical properties in the weaker orientations and reduce the overall anisotropy is accepted.

The higher strength and fracture resistance for the YX orientation can be attributed to the difficulty of the crack propagating across the ceramic columns that were templated by the ice crystals that formed along the y-direction, identified as lighter and darker vertical banding in Fig. 1a. In this case, the crack makes frequent, small changes in the crack plane (Fig. 4c) creating a more tortuous fracture process that results in higher strength and toughness. For the XY and XZ orientations, without ultrasound there are few barriers to crack propagation as the crack propagates parallel to, or kinks around, the ceramic columns that were templated by the growth of the ice crystals, as is shown in Fig. 4. It was observed that there was a significant improvement of the fracture resistance for the XY and XZ orientations with the addition of the relatively dense layers produced by ultrasound (Figs. 2b and 3). The significant change in the freeze-cast material microstructure with the application of ultrasound frequency was the introduction of the denser ceramic layers oriented in the x-z plane perpendicular to the freeze front direction (Fig. 1e) [28]. The relatively dense regions are produced by ultrasound inhibiting the redistribution of the ceramic particles present in the colloid slurry suspension. In the lamellar region, the ceramic particles are pushed into the spaces between the crystals during the ice crystal growth process. The ultrasound application reduces the movement of the ceramic particles at the nodes of the standing ultrasound waves resulting in a denser layer of ceramic that sit on the x-z plane between lamellar regions (Fig. 1d and e). The location and scale of the relatively dense and lamellar regions are directly related to the ultrasound operating frequency [28]. At higher ultrasound operating frequencies, TiO_2 particles were concentrated in smaller areas and the separation between repeating layers decreased. Such relatively dense layers are not present in the 0 MHz group which consists entirely of a lamellar structure oriented along the freezing direction (Fig. 1b and c). Thus, the enhanced properties for the XY and XZ orientations with the ultrasound treatment are attributed to the crack needing to cut through the denser layers for those orientations. In contrast, for the YX orientation the crack is able to propagate through the lamellar structure for all samples mostly avoiding the relatively dense layers produced by ultrasound. Thus, fracture resistance for the YX orientation is less sensitive to the ultrasound treatment.

The strength of a brittle material is governed by both the fracture resistance (*R*-curve) and the critical flaw that initiates fracture. If the critical flaw size, shape, and orientation is known for each sample from fractography, or alternatively can be assumed to be constant across all samples, then a mathematical relationship between the strength and *R*-curve is straightforward, as described in Ref. [35]. However, in the present work the denser layers were formed by a redistribution of the ceramic particles caused by the ultrasound. Thus, the remaining lamellar regions in the ultrasound groups are somewhat depleted in ceramic phase compared to the 0 MHz group, giving a more porous structure (that was were filled with two-part epoxy) in the immediate vicinity of the denser layers. The effect of the enhanced porosity of the lamellar regions is clearly observed for the strength in the YX orientation where there is a significant reduction of strength after ultrasound. The toughness for the YX orientation didn't change much, or increased somewhat, with ultrasound indicating that the strength reduction was instead caused by the introduction of larger porosity in the lamellar regions that acts as the critical flaw sites. Furthermore, the strength decrease was largest for the 0.699 MHz condition where previous work has measured that the denser layers are relatively thickest [28], thus causing the most ceramic depletion from the adjoining lamellar layers. In contrast, the strength values were quite similar for the 1.39 and 2.097 MHz samples where the dense layer thicknesses were previously reported to be similar with no statistically significant difference [28].

For the XY and XZ orientations, the fracture resistance nearly doubles as the ultrasound frequency increases to 2.097 MHz and this coincides with a less dramatic increase in strength. Here it is deduced that the increase in fracture toughness with ultrasound is sufficient to offset any increases in the critical flaw size and give an overall higher fracture strength. Thus, the net result for the 2.097 MHz samples is a compromise in strength and toughness for all orientations with anisotropy ratios of 1.3 and 1.2 for strength and toughness, respectively.

5. Conclusion

The freeze-casting epoxy-ceramic composite material showed strongly anisotropic strength and fracture resistance in the absence of applied ultrasound. The higher strength and fracture resistance in the YX orientation was associated with the higher resistance for cracks to propagate across the ceramic columns formed along the y-direction during the freeze casting process. The application of ultrasound frequencies from 0.699 to 2.097 progressively improved the mechanical properties for the weaker orientations (XY and XZ) and reduced the overall anisotropy. The enhanced fracture resistance for the XY and XZ orientations was attributed to crack deflection due to the addition of relatively dense ceramic layers produced by ultrasound. The more isotropic strength response for the ultrasound freeze cast samples opens opportunities for these materials to be applied in applications where they are expected to function under multidirectional and/or variable direction loadings.

Declaration of competing interest

The authors declare that they have no known competing financial interests or personal relationships that could have appeared to influence the work reported in this paper.

Acknowledgements

This work was supported in part by the National Science Foundation of the United States under grant CMMI # 1660979. The authors acknowledge the facilities and the scientific and technical assistance of Microscopy Australia at the Electron Microscope Unit (EMU) within the Mark Wainwright Analytical Centre (MWAC) at UNSW Sydney, Australia.

References

[1] E. Landi, F. Valentini, A. Tampieri, Porous hydroxyapatite/gelatine scaffolds with ice-designed channel-like porosity for biomedical applications, Acta Biomater. 4 (2008) 1620–1626.
[2] P. Divakar, K.L. Moodie, E. Demidenko, P.J. Hoopes, U.G.K. Wegst, Quantitative evaluation of the in vivo biocompatibility and performance of freeze-cast tissue scaffolds, Biomed. Mater. 15 (2020), 055003.
[3] S. Deville, E. Saiz, A.P. Tomsia, Freeze casting of hydroxyapatite scaffolds for bone tissue engineering, Biomaterials 27 (2006) 5480–5489.
[4] T. Um, S.K. Wilke, H. Choe, D.C. Dunand, Effects of pore morphology on the cyclical oxidation/reduction of iron foams created via camphene-based freeze casting, J. Alloys Compd. 845 (2020) 156278.
[5] P.J. Lloreda-Jurado, S.K. Wilke, K. Scotti, A. Paul-Escolano, D.C. Dunand, R. Sepulveda, Structure-processing relationships of freeze-cast iron foams fabricated with various solidification rates and post-casting heat treatment, J. Mater. Res. 35 (2020) 2587–2596.
[6] J.I. Roscow, Y. Zhang, M.J. Krasny, R.W.C. Lewis, J. Taylor, C.R. Bowen, Freeze cast porous barium titanate for enhanced piezoelectric energy harvesting, J. Phys. D 51 (2018) 225301.
[7] I. Nelson, J. Varga, P. Wadsworth, M. Mroz, J.J. Kruzic, O. Kingstedt, S.E. Naleway, Helical and Bouligand porous scaffolds fabricated by dynamic low strength magnetic field freeze casting, J. Occup. Med. 72 (2020) 1498–1508.
[8] D. Ghosh, M. Banda, J.E. John, D.A. Terrones, Dynamic strength enhancement and strain rate sensitivity in ice-templated ceramics processed with and without anisometric particles, Scripta Mater. 154 (2018) 236–240.
[9] M. Banda, S. Akurati, D. Ghosh, Governing role of the ratio of large platelet particles to ultrafine particles on dynamic and quasistatic compressive response and damage evolution in ice-templated alumina ceramics, J. Mater. Res. 35 (2020) 2870–2886.
[10] I. Nelson, S.E. Naleway, Intrinsic and extrinsic control of freeze casting, Journal of Materials Research and Technology 8 (2019) 2372–2385.

[11] S. Deville, Freeze-casting of porous ceramics: a review of current achievements and issues, Adv. Eng. Mater. 10 (2008) 155–169.
[12] S. Deville, Ice-templating, freeze casting: beyond materials processing, J. Mater. Res. 28 (2013) 2202–2219.
[13] S. Deville, Freeze-casting of porous biomaterials: structure, properties and opportunities, Materials 3 (2010) 1913–1927.
[14] K.L. Scotti, D.C. Dunand, Freeze casting – a review of processing, microstructure and properties via the open data repository, FreezeCasting.net, Progress in Materials Science 94 (2018) 243–305.
[15] P.M. Hunger, A.E. Donius, U.G.K. Wegst, Structure-property-processing correlations in freeze-cast composite scaffolds, Acta Biomater. 9 (2013) 6338–6348.
[16] M.M. Porter, R. Imperio, M. Wen, M.A. Meyers, J. McKittrick, Bioinspired scaffolds with varying pore architectures and mechanical properties, Adv. Funct. Mater. 24 (2013) 1978–1987.
[17] T.J. Kuo, L.M. Rueschhoff, M.B. Dickerson, T.A. Patel, K.T. Faber, Hierarchical porous SiOC via freeze casting and self-assembly of block copolymers, Scripta Mater. 191 (2021) 204–209.
[18] H.K. Chang, P.-Y. Chen, Synthesis of silica-based scaffolds with high porosity and controllable microstructure by a sintering-free sol-gel/freeze-casting hybrid method under mild conditions, Journal of Materials Research and Technology 9 (2020) 16167–16178.
[19] S. Roy, A. Wanner, Metal/ceramic composites from freeze-cast ceramic preforms: domain structure and elastic properties, Compos. Sci. Technol. 68 (2008) 1136–1143.
[20] M.E. Launey, E. Munch, D.H. Alsem, E. Saiz, A.P. Tomsia, R.O. Ritchie, A novel biomimetic approach to the design of high-performance ceramic-metal composites, J. R. Soc. Interface 7 (2010) 741–753.
[21] C. Ferraro, S. Meille, J. Rethore, N. Ni, J. Chevalier, E. Saiz, Strong and tough metal/ceramic micro-laminates, Acta Mater. 114 (2018) 202–215.
[22] M.J. Garnier, D.C. Dunand, Ni-Al_2O_3 nacre-like composites through hot-pressing of freeze-cast foams, Mater. Sci. Eng. 743 (2019) 190–196.
[23] Y. Tang, S. Qiu, Q. Miao, C. Wu, Fabrication of lamellar porous alumina with axisymmetric structure by directional solidification with applied electric and magnetic fields, J. Eur. Ceram. Soc. 36 (2016) 1233–1240.
[24] Z. Cheng, K. Zhao, Z.P. Wu, Structure control of hydroxyapatite ceramics via an electric field assisted freeze casting method, Ceram. Int. 41 (2015) 8599–8604.
[25] M.M. Porter, M. Yeh, J. Strawson, T. Goehring, S. Lujan, P. Siripasopsotorn, M. A. Meyers, J. McKittrick, Magnetic freeze casting inspred by nature, Mater. Sci. Eng. 556 (2012) 741–750.
[26] I. Nelson, L. Gardner, K. Carlson, S.E. Naleway, Freeze casting of iron oxide subject to a tri-axial nested Helmholtz-coils driven uniform magnetic field for tailored porous scaffolds, Acta Mater. 173 (2019) 106–116.
[27] I. Nelson, T.A. Ogden, S. Al Khateeb, J. Graser, T.D. Sparks, J.J. Abbott, S. E. Naleway, Freeze-casting of surface-magnetized iron(II,III) oxide particles in a uniform static magnetic field generated by a Helmholtz coil, Adv. Eng. Mater. 21 (2019) 1801092.
[28] M. Mroz, J. Rosenberg, C. Acevedo, J.J. Kruzic, B. Raeymaekers, S.E. Naleway, Ultrasound freeze-casting of a biomimetic layered microstructure in epoxy-ceramic composite materials to increase strength and hardness, Materialia 12 (2020) 100754.
[29] T.A. Ogden, M. Prisbrey, I. Nelson, B. Raeymaekers, S.E. Naleway, Ultrasound freeze casting: fabricating bioinspired porous scaffolds through combining freeze casting and ultrasound directed self-assembly, Mater. Des. 164 (2019) 107561.
[30] R.K. Nalla, J.H. Kinney, R.O. Ritchie, Effect of orientation on the in vitro fracture toughness of dentin: the role of toughening mechanisms, Biomaterials 24 (2003) 3955–3968.
[31] C.B. Tanaka, Y. Zhou, B. Gludovatz, J.J. Kruzic, Anisotropic fracture resistance of avian eggshell, Journal of the Mechanical Behavior of Biomedical Materials 110 (2020) 103888.
[32] E.A. Zimmermann, B. Gludovatz, E. Schaible, B. Busse, R.O. Ritchie, Fracture resistance of human cortical bone across multiple length-scales at physiological strain rates, Biomaterials 35 (2014) 5472–5481.
[33] K. Bertoldi, D. Bigoni, W.J. Drugan, Nacre: an orthotropic and bimodular elastic material, Compos. Sci. Technol. 68 (2008) 1363–1375.
[34] S. Akurati, J. Marin, B. Gundrati, D. Ghosh, Assessing the role of loading direction on the uniaxial compressive response of multilayered ice-templated alumina-epoxy composites, Materialia 14 (2020) 100895.
[35] J.J. Kruzic, R. Satet, M.J. Hoffmann, R.M. Cannon, R.O. Ritchie, The utility of R-curves for understanding fracture toughness-strength relations in bridging ceramics, J. Am. Ceram. Soc. 91 (2008) 1986–1994.
[36] V. Naglieri, B. Gludovatz, A.P. Tomsia, R.O. Ritchie, Developing strength and toughness in bio-inspired silicon carbide hybrid materials containing a compliant phase, Acta Mater. 98 (2015) 141–151.
[37] S. Askarinejad, N. Rahbar, Mechanics of bioinspired lamellar structured ceramic/polymer composites: experiments and models, Int. J. Plast. 107 (2018) 122–149.
[38] M.Y. Zhang, D. Jiao, G.Q. Tan, J. Zhang, S.G. Wang, J.Y. Wang, Z.Q. Liu, Z. F. Zhang, R.O. Ritchie, Strong, fracture-resistant biomimetic silicon carbide composites with laminated interwoven nanoarchitectures inspired by the crustacean exoskeleton, ACS Applied Nano Materials 2 (2019) 1111–1119.
[39] D. Jiao, J. Zhang, Y.Y. Liu, X.G. Liu, Q. Zhang, S.F. Tang, Z.Q. Liu, Z.F. Zhang, Hierarchical toughening of bioinspired nacre-like hybrid carbon composite, Carbon 171 (2021) 409–416.
[40] ASTM C1161-18. Standard Test Method for Flexural Strength of Advanced Ceramics at Ambient Temperature, ASTM International, West Conshohocken, PA, 2018.
[41] S. Fünfschilling, T. Fett, S.E. Gallops, J.J. Kruzic, R. Oberacker, M.J. Hoffmann, First- and second-order approaches for the direct determination of bridging stresses from R-curves, J. Eur. Ceram. Soc. 30 (2010) 1229–1236.